JGR Space Physics

RESEARCH ARTICLE
10.1029/2018JA026403

Origin of the Extended Mars Radar Blackout of September 2017

Beatriz Sánchez–Cano[1], Pierre-Louis Blelly[2], Mark Lester[1], Olivier Witasse[3], Marco Cartacci[4], Roberto Orosei[5], Hermann Opgenoorth[6,1], Robert Lillis[7], François Leblanc[8], Stephen E. Milan[1], Philip Conroy[3], Nicolas Floury[3], John M. C. Plane[9], Andrea Cicchetti[4], Raffaella Noschese[4], and Andrew J. Kopf[10]

[1]Radio and Space Plasma Physics Group, Department of Physics and Astronomy, University of Leicester, Leicester, UK, [2]Institut de Recherche en Astrophysique et Planétologie, Toulouse, France, [3]ESTEC, European Space Agency, Noordwijk, Netherlands, [4]Istituto di Astrofisica e Planetologia Spaziali, Istituto Nazionale di Astrofisica, Rome, Italy, [5]Istituto di Radioastronomia, Istituto Nazionale di Astrofisica, Bologna, Italy, [6]Department of Physics, Umeå University, Umea, Sweden, [7]Space Sciences Laboratory, University of California, Berkeley, CA, USA, [8]LATMOS/CNRS, Sorbonne Université, UVSQ, CNRS, Paris, France, [9]School of Chemistry, University of Leeds, Leeds, UK, [10]Department of Physics and Astronomy, University of Iowa, Iowa City, IA, USA

Key Points:
- A large space weather event caused negatively impacted radar performance for 10 days
- Solar electron precipitation created a low ionospheric layer at ~90 km on the nightside
- The nightside ionization is comparable to dayside values

Supporting Information:
- Supporting Information S1

Correspondence to:
B. Sánchez–Cano,
bscmdr1@leicester.ac.uk

Citation:
Sánchez–Cano, B., Blelly, P.-L., Lester, M., Witasse, O., Cartacci, M., Orosei, R., et al. (2019). Origin of the extended Mars radar blackout of September 2017. *Journal of Geophysical Research: Space Physics*, *124*, 4556–4568. https://doi.org/10.1029/2018JA026403

Received 17 DEC 2018
Accepted 3 MAY 2019
Accepted article online 9 MAY 2019
Published online 6 JUN 2019

Abstract The Mars Advanced Radar for Subsurface and Ionosphere Sounding (MARSIS) onboard Mars Express, which operates between 0.1 and 5.5 MHz, suffered from a complete blackout for 10 days in September 2017 when observing on the nightside (a rare occurrence). Moreover, the Shallow Radar (SHARAD) onboard the Mars Reconnaissance Orbiter, which operates at 20 MHz, also suffered a blackout for three days when operating on both dayside and nightside. We propose that these blackouts are caused by solar energetic particles of few tens of keV and above associated with an extreme space weather event between 10 and 22 September 2017, as recorded by the Mars Atmosphere and Volatile EvolutioN (MAVEN) mission. Numerical simulations of energetic electron precipitation predict that a lower O_2^+ nighttime ionospheric layer of magnitude ~10^{10} m^{-3} peaking at ~90-km altitude is produced. Consequently, such a layer would absorb radar signals at high frequencies and explain the blackouts. The peak absorption level is found to be at 70-km altitude.

Plain Language Summary Several instrument operations, as well as communication systems with rovers at the surface, depend on radio signals that propagate throughout the atmosphere of Mars. This is the case also for two radars that are currently working in Mars' orbit, sounding the ionosphere, surface, and subsurface of the planet. In mid-September 2017, a powerful solar storm hit Mars, producing a large amount of energetic particle precipitation over a 10-day period. We have found that high-energy electrons ionized the atmosphere of Mars, creating a dense layer of ions and electrons at ~90 km on the Martian nightside. This layer attenuated radar signals continuously for 10 days, stopping the radars to receive any signal from the planetary surface. In this work, we assess the properties of this layer in order to understand the implications of this kind of phenomenon for radar performance and communications.

1. Introduction

Precipitation of energetic charged particles as well as ablation of interplanetary dust particles can produce a prompt rise in the electron density of the ionosphere of Mars below 100 km, where the plasma density is typically very low (e.g., Espley et al., 2007; Lillis et al., 2018; Molina-Cuberos et al., 2003; Pesnell & Grebowsky, 2000). At these altitudes, the electron-neutral collision frequency is of the same order as the high frequency (HF) of the radars. Therefore, if electrons are present, radio waves at these frequencies can be attenuated, or in the worst case, totally absorbed. Consequently, a severe degradation of performance of radio-based instruments such as radars and sounders as well as navigation and communication systems can occur (e.g., Withers, 2011). Previous research has shown that radio blackouts at Mars may occur more often than expected (e.g., Espley et al., 2007) and with long-lasting effects, especially after strong space weather activity. Therefore, a good understanding of this phenomenon is needed on the eve of the era of the human exploration of Mars.

It is known that solar energetic particles (SEPs; e.g., Espley et al., 2007; Němec et al., 2014), corotating interaction regions (CIRs; e.g., Morgan et al., 2010), interplanetary coronal mass ejections (ICMEs; e.g., Andrews et al., 2016; Campbell et al., 2014; Morgan et al., 2014), meteoric showers (e.g., Molina-Cuberos et al., 2003; Pesnell & Grebowsky, 2000; Witasse et al., 2001), and areas over closed crustal magnetic field lines (e.g., Němec et al., 2015) can cause some radar disruptions. All these scenarios are believed to produce a rise in the electron density of the lower ionosphere below 100 km, where even a small amount of extra ionization significantly increases the signal attenuation (e.g., Nielsen et al., 2007). Some work suggests that solar protons of tens of MeV could be the cause for these absorption layers, similar to the polar cap absorption events at Earth (e.g., Morgan et al., 2006; Sheel et al., 2012). However, electron precipitation is considered to be the dominant source of ionization in Mars' nightside upper atmosphere (e.g., Fillingim et al., 2007; Fox et al., 1993; Leblanc et al., 2006; Lillis et al., 2011, 2018; Lillis & Fang, 2015), together with plasma transport.

On September 2017, after one of the strongest space weather energetic particle events of the latest 15 years hit Mars, the Mars Advanced Radar for Subsurface and Ionosphere Sounding (MARSIS) on board Mars Express (MEX) and the Shallow Radar (SHARAD) onboard the Mars Reconnaissance Orbiter (MRO) suffered long-lasting signal blackouts for several days. It appears that this blackout event was caused by a global absorption layer, including the deep-nightside region (total darkness). The locations of the blackouts are shown in Figure 1 and in the supporting information file. Its long duration is itself remarkable, as it suggests that a near-permanent lower ionospheric layer globally stopped HF communications with the surface for several days. Moreover, the fact that the layer was also formed on the deep nightside is of great interest, as radars typically work better in that region because the critical plasma frequency of the ionosphere (as determined by the peak electron density) is typically well below the radar carrier frequency (e.g., Cartacci et al., 2013, 2018; Mouginot et al., 2008; Safaeinili et al., 2003, 2007; Sánchez-Cano, Morgan, et al., 2015); that is, the ionosphere is very tenuous (Girazian, Mahaffy, Lillis, Benna, Elrod, Jakosky, 2017; Girazian, Mahaffy, Lillis, Benna, Elrod, Jakosky, Fowler, et al., 2017).

The objective of this work is to assess the properties of such a putative lower ionospheric layer that was created on the deep nightside during September 2017. The main aim is to understand which ionizing agent can create such layers, as well as the electron densities required at different altitudes to inhibit the radar link to the ground.

2. Space Weather Context

Figures 2a–2c display Mars Atmosphere and Volatile EvolutioN (MAVEN) mission observations as a function of time for the period 4–29 September 2017. The irradiance data are taken from the Extreme-Ultraviolet (EUV) monitor in the wavelengths 0.1–7 nm (Eparvier et al., 2015), and the ion and electron differential flux spectra are from the Solar Energetic Particle instrument (hereinafter MAVEN-SEP) (Larson et al., 2015). Only data from the MAVEN-SEP1 sensor's forward look direction have been plotted, although we note that both forward and rear look directions show similar observations.

The Active Region (AR) 12673 at the western limb of the solar disk during September 2017 was very productive in terms of Earth-directed X-class solar flares and ICMEs (e.g., Jiggens et al., 2018; Redmon et al., 2018). The same AR also emitted a X8.2-class flare on 10 September 2017 starting at ~15:35 UT and peaking at ~16:06 UT, and released a powerful CME at ~15:54 UT (Guo et al., 2018; Lee et al., 2018). At Mars, 160° from Earth in the ecliptic plane, the peak of the flare was observed at 16:11 (~5 min after Earth; Figure 2a). SEP electrons (20–200 keV) started to arrive at Mars at ~19:20 UT (~3 hr later; Figure 2c), and ions (20 keV–6 MeV) at ~22:00 UT (~6 hr later; Figure 2b). Lee et al. (2018) showed that 15–220 MeV SEP protons also penetrated the MAVEN-SEP instrument from ~22:00 UT, although direct energy flux measurements are not available as the instrument is optimized to measure 20 keV–6 MeV protons. Both SEP electrons and ions (Figures 2b and 2c) show a sharp flux increase on 12 September 2017 (reddish colors) when the ICME shock passed over Mars. After that, SEP electrons gradually decreased over 13 days until 23 September, but with a small enhancement on 18 September caused by another solar flare (Figures 2a and 2c). In contrast, SEP ions sharply decreased on 14 September when the ICME completed its passage past Mars. After that, the ion flux was very low until 20 September, when there was a further notable rise (reddish colors) most probably

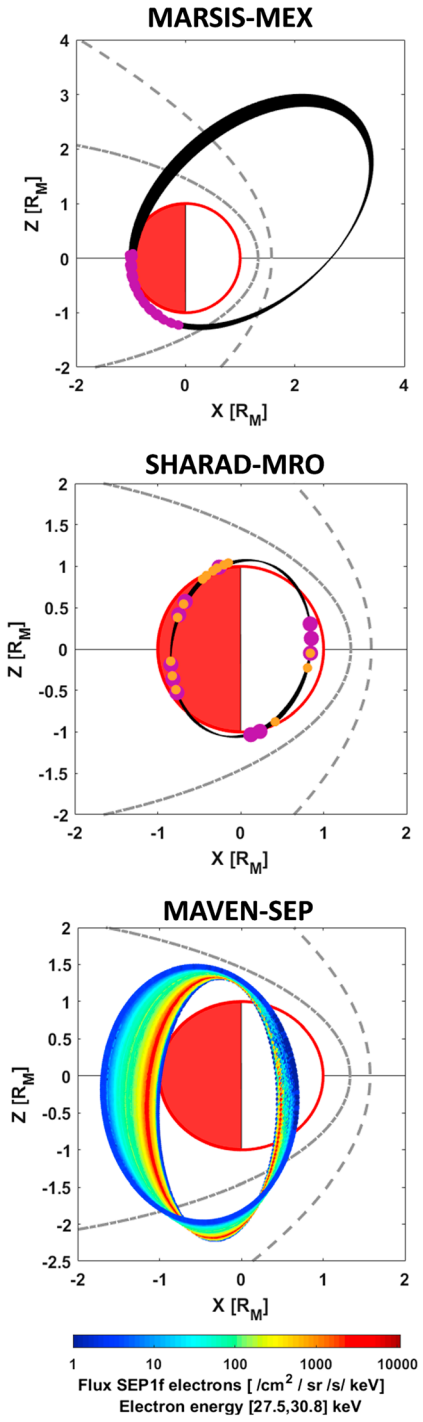

Figure 1. MEX, MRO, and MAVEN orbits in the *z*-*x* MSO plane. The rest of the orbital planes as well as the latitude-longitude coordinates can be found in the supporting information. The Sun is to the right. A grey dash-dotted line indicates the magnetic pileup boundary position (Edberg et al., 2008), and a grey dashed line the bow shock position (Hall et al., 2016). (top panel) Blackout locations of MARSIS-MEX radar in purple circles. (middle panel) Total blackout locations of SHARAD-MRO radar in purple circles, and partial blackouts (highly blurry surface observations) in orange circles. (bottom panel) MAVEN-SEP flux observations (color-coded) along its orbit. The electron flux used in this figure correspond to the energy interval 27.5–30.8 keV.

caused by the passage of the flank of another ICME magnetically well connected to Mars (see ENLIL run at https://ccmc.gsfc.nasa.gov/database_SH/Leila_Mays_120817_SH_9.php; Lee et al., 2018).

3. Radar Attenuation

3.1. MARSIS and SHARAD Observations

The MARSIS radar on board Mars Express (Chicarro et al., 2004) is a nadir-looking pulse-limited radar sounder with a 40-m dipole antenna. The radar has two different operational modes (e.g., Orosei et al., 2015; Picardi et al., 2004): (1) a subsurface mode designed to sound the surface and subsurface of the planet with frequencies centered at 1.8, 3, 4, and 5 MHz. Two different frequencies are transmitted in sequence with a small delay (450 μs) between them to avoid the possibility of overlapping during the receiving phase. The selection of the transmitted frequencies mainly depends on the solar zenith angle (SZA) conditions at the time of the observations. Both transmitted bandwidths are always chosen to be well above the critical plasma frequency of the ionosphere below, in order to be able to propagate with the smallest possible degradation. For this study, 3 and 4 MHz were the operational MARSIS frequencies since the observations were planned to be collected during the nightside. (2) An Active Ionospheric Sounding (AIS) mode designed to sound the topside ionosphere from the spacecraft location up to the critical plasma frequency of the ionosphere with a sweep of frequencies between 0.1 and 5.5 MHz. In AIS mode, the radar frequencies can also be reflected from the Martian surface if the carrier frequency is larger than the critical plasma frequency, and the total electron content of the bottomside ionosphere is thin enough not to attenuate the signals. Complementary to MARSIS, the SHARAD radar onboard Mars Reconnaissance Orbiter (Zurek & Smrekar, 2007) also sounds the Martian surface-subsurface with a linear chirp signal centered at 20 MHz and a bandwidth of 10 MHz (Seu et al., 2004), which is always higher than the critical plasma frequency.

Figures 3a–3b show several radargrams from MARSIS and SHARAD. A radargram is a 2-D backscattered power image of the surface-subsurface reflections built from the radar measurements along the orbit. Time delay is typically plotted on the vertical axis and the along-track distance on the horizontal axis. The brightness of the pixel is a function of the strength of the echo measured in decibels (dB). During September 2017, MARSIS was sampling the southern hemisphere of Mars on the deep nightside, although not on every MEX orbit. SHARAD in contrast was sampling both dayside and nightside, and both hemispheres due to MRO's Sun-synchronous low 250 × 320 km orbit. Different symbols in Figure 2d show the timing when MARSIS and SHARAD were in operation. Empty symbols indicates when both radars observed a reflection from the surface, and filled symbols when the surface reflection was not received (i.e., the radars were transmitting but not receiving signals). In addition, a green diamond indicates when the surface reflection was highly blurry for the SHARAD radar. While the blackout lasted at least ~10 days for both MARSIS operational modes, the blackout lasted only ~3 days for SHARAD because radio absorption processes are frequency-dependent (see section 4). Figure 2 clearly demonstrates that SEP electrons were present during the entire period of the radar blackout and therefore suggests that precipitating

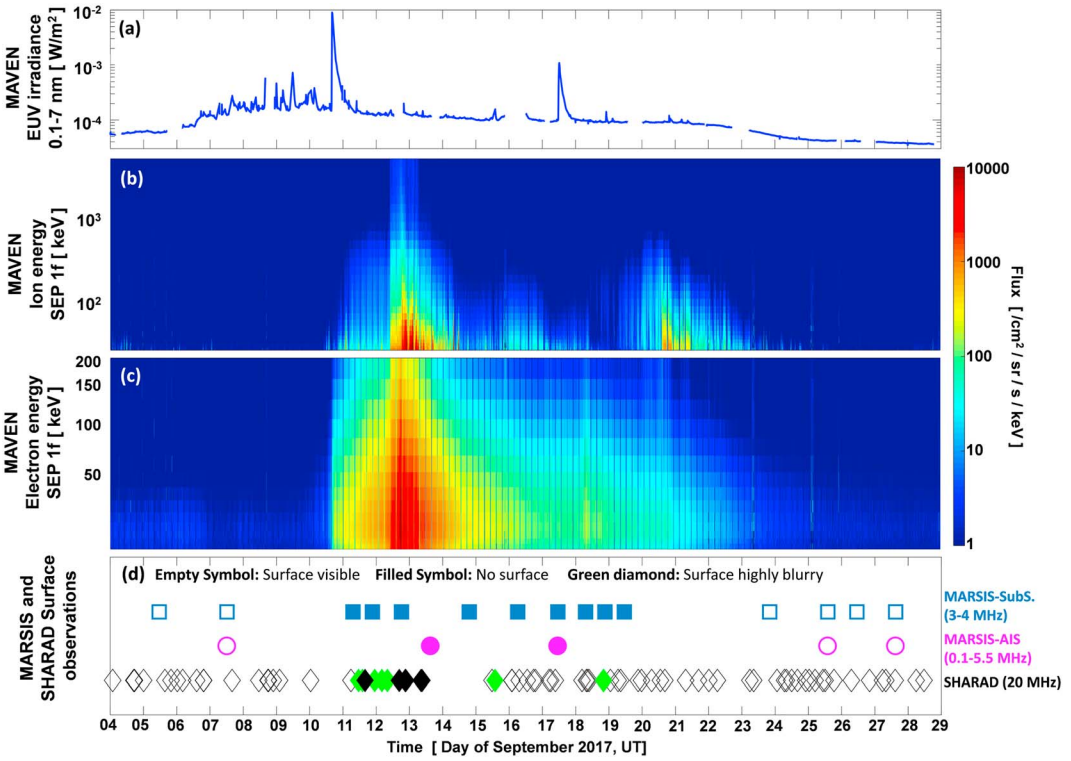

Figure 2. (a) MAVEN-EUV irradiance observations of wavelength 0.1–7 nm. (b) MAVEN-SEP ion differential flux spectra. (c) MAVEN-SEP electron differential flux spectra. (d) Each symbol denotes when MARSIS and SHARAD were in operation. Empty symbols designate the cases when the surface was observed, and filled symbols when was not observed. The exceptions are green diamonds that indicate the times when SHARAD observed a highly blurry surface.

electrons, rather than ions, were responsible for the creation of a lower nightside ionospheric layer that absorbed the radar signals (see section 6 for details).

3.2. Estimation of the Attenuation

To estimate the MARSIS radar attenuation during this event, we have compared the signal power versus delay time for orbit 17362 (one of those affected by the blackout) with previous orbits close in time when

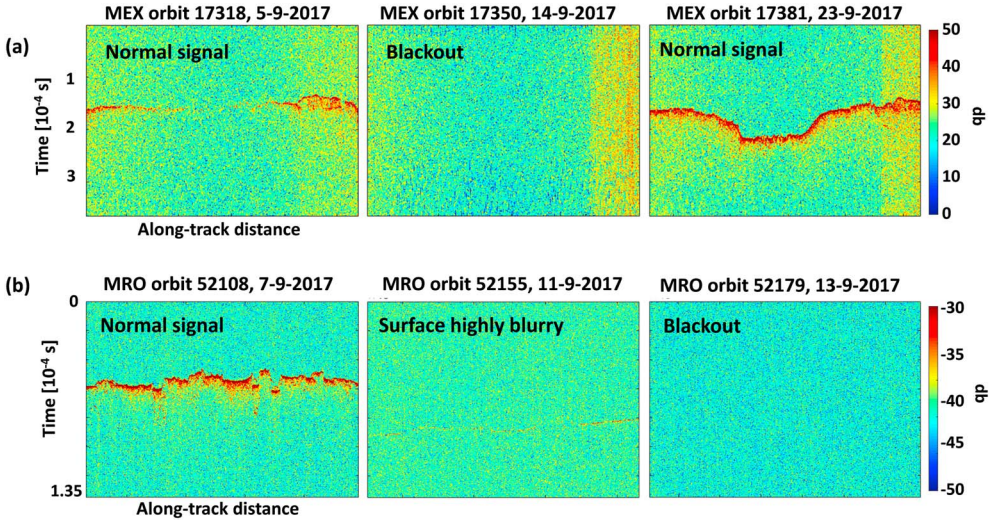

Figure 3. Radargram examples showing normal surface reflections, blackouts, and partial blackouts (surface highly blurry). (a) MARSIS radargrams. (b) SHARAD radargrams.

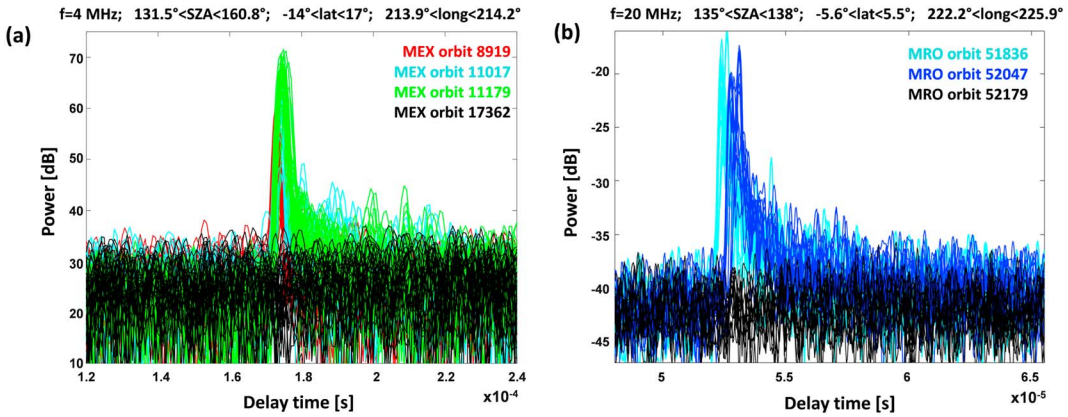

Figure 4. (a) MARSIS power signal versus delay time for several orbits over the same region. (b) SHARAD power signal versus delay time for several orbits over the same region.

the radars operated at the same frequency, on the nonilluminated nightside (SZA >130°), and over the same region of the planet. Orbit 17362 was chosen because the surface area tracked by MARSIS is sufficiently flat for a region of the southern hemisphere, in order to minimize the topography and composition effect on the signal power reflected back to the radar. Only radargrams from the nadir-pointing direction are used in this analysis. Peaks at $1.7–1.9 \times 10^{-4}$ s in Figure 4a correspond to the power signal reflection of the Martian surface in orbits not affected by the blackout. The average power signal of the surface reflection in this area is 60 dB for 4 MHz, and 59 dB for 3 MHz. During the space weather event (black profiles; Figure 4a), the MARSIS signal power fell to the background noise level that was on average 24 ± 9 dB for 4 MHz and 25 ± 9 dB for 3 MHz for the whole orbit. We define the noise uncertainty as 1.5 times the standard deviation of the noise in Figures 4a and 4b. The proposed noise threshold is a reasonable solution in order to identify with good accuracy the leading edge of the signal that is critical for correct estimations of the signal travel time. Therefore, after considering the difference between the nominal power signal and the noise level, the radar signals were attenuated by at least 36 ± 9 dB for 4 MHz and 34 ± 9 dB for 3 MHz. Assuming that this attenuation operates in both directions (spacecraft-surface-spacecraft), the lower limit attenuation that we can estimate for one way is at least 18 ± 9 and 17 ± 9 dB for 4 and 3 MHz, respectively.

The same procedure was carried out for the SHARAD radar at 20 MHz. Previous orbits over the same flat region of orbit 52179 were compared (Figure 4b), obtaining a two-way attenuation of 19.0 ± 3.3 dB, and a one-way attenuation of 9.5 ± 3.3 dB. We note that the sign of the MARSIS and SHARAD power signals are different because both instruments have a different reference level. This is not an issue for our study, as we are estimating the absolute value of the attenuation on each radar separately.

4. Radio Attenuation Theory

A radar signal (electromagnetic wave) crossing the Martian ionosphere can experience four different effects (Campbell et al., 2014; Safaeinili et al., 2003): (1) an increase in the time delay with respect to that expected from the speed of light in vacuum, (2) distortion of the signal phase due to the frequency dependence of the refractive index (radar signals close to the critical frequency of the ionosphere), (3) attenuation of the signal amplitude that is controlled by thermal electron collisions with the neutrals, and (4) Faraday rotation effects over strong crustal magnetic field regions (this effect is minor compared to attenuation (Safaeinili et al., 2003)). In this work, radar signals are expected to be totally lost mainly due to attenuation processes since the operational frequencies of both radars are much larger than the expected ionospheric critical frequency of the normal ionosphere (see section 5), while this new absorbing layer is expected to be formed below 100 km where the neutral atmosphere is denser. Nevertheless, we note that for those cases when the surface is highly blurry (Figure 4b), large signal phase delays must have been as important as absorption processes.

Neglecting any effect of Mars' crustal magnetic fields, radio waves can be attenuated during their propagation through the ionosphere as described by equation (1). We neglect the effect of the crustal fields because their influence on radio-propagation can be considered weak (Nielsen et al., 2007), and also, because the

radio blackouts occurred everywhere over the planet and not only over crustal field areas (see Figure 1 and supporting information). Combining equations (1) and (2), the attenuation can be rewritten as equation (3).

$$A(h) = 8.686\ \frac{2\,\pi f}{c}\ \mathrm{Im}\left(\sqrt{1-\frac{(2\,\pi f_P)^2}{(2\,\pi f)^2 - i\,2\,\pi\nu f}}\right) \tag{1}$$

$$f_P = 8.98\ \sqrt{N_e(h)} \tag{2}$$

$$A(h) = 4.61{\times}10^7\ N_e(h)\ \frac{\nu(h)}{(2\,\pi f)^2 + \nu^2(h)} \tag{3}$$

where A is the attenuation in dB/m; ***Im*** is the imaginary term; f and f_P are the carrier and plasma frequencies respectively in Hz; c is the speed of light; ν is the momentum-transfer electron-neutral collision frequency in s^{-1}, and N_e is the electron density in m^{-3}.

In the lower ionosphere, the main neutral component is carbon dioxide (CO_2), and therefore, ν can be set equal to the electron-CO_2 collision frequency (Witasse et al., 2001). In this study, we use the well-accepted ν formula described by Schunk and Nagy (2009), using equation (4) which is based on Itikawa (1978), who considers the electron temperature, T_e, and CO_2 neutral density, n, as inputs.

$$\nu\,(e^- - CO_2) = 3.68\times10^{-8}\ n\ \left(1 + 4.1\times10^{-11}\ |4500 - T_e|^{2.93}\right) \tag{4}$$

Since ν *is* directly proportional to n, ν increases with decreasing altitude, and this results in a larger radar absorption in the lower atmosphere. Consequently, even a very small ionospheric layer at low altitude has a larger effect on the attenuation than the main dayside layer peaking at 130–140 km (Witasse et al., 2001).

5. Ionospheric Modeling

In order to assess the main properties of the lower ionospheric layer created during this event, we use the Mars version of the numerical/physical Institut de Recherche en Astrophysique et Planétologie (IRAP) plasmasphere-ionosphere model (IPIM) (Marchaudon & Blelly, 2015). IPIM is based on the TRANSCAR and TRANSMARS codes (e.g., Blelly et al., 1996, 2005; Morel et al., 2004; Ramírez-Nicolás et al., 2016; Sánchez-Cano, Lester, et al., 2015; Sánchez-Cano et al., 2018; Witasse, 2000; Witasse et al., 2002, 2003), in which transport equations for the ionized species are based on a 16 moment approximation, and the suprathermal electron fluxes are computed after solving their steady state transport equation. The model also takes into account for primary and secondary collisions with the neutrals and excitation and ionization processes, either by solar radiation illumination or electron impact (Blelly et al., 2019). The Mars version uses the Mars Climate Database (MCD) (version 5.3) as input for neutral atmospheric conditions (e.g., Forget et al., 1999; Millour et al., 2015), and it includes the six major ion species (O_2^+, NO^+, O^+, CO_2^+, N_2^+, and H^+) in the Martian ionosphere. Other ion species are not considered in this study because their densities are several orders of magnitude smaller. The simulation was performed for the prevailed conditions during the MARSIS observations (i.e., similar solar activity level, solar zenith angle, and planet location) on 10 September 2017, at 23:00:00 UT, at the beginning of the Mars space weather event. Since Figure 2 strongly suggests that electrons were responsible for this blackout, a flux of downward precipitating electrons at 500 km was included in the model as a source of ionization (Figure 5a). This precipitating electron flux was fitted only to the MAVEN-SEP observations for the higher energies (above 20 keV) as we are sure that these electrons are not originating from Martian environment. We did not considered MAVEN Solar Wind Electron Analyzer (SWEA) observations at low altitude because they were taken when MAVEN was on the dayside, and there was a strong risk that we account for photoelectrons in the precipitation flux when this simulation is focused on the deep nightside. The simulation considers different scattering angles with respect to the vertical, being positive for the downward direction and negative for the upward direction. Figure 5a also shows the electron flux at two different altitudes. At 500 km, most of the flux precipitates in the downward direction with almost no scattering due to upper boundary conditions for the flux and low atmospheric densities. At 70 km, the flux is isotropic due to scatter on a denser atmosphere. Only secondary electrons remain at lower energies (~1–50 eV). Although the input flux is mainly in the range ~10 keV (based on MAVEN-

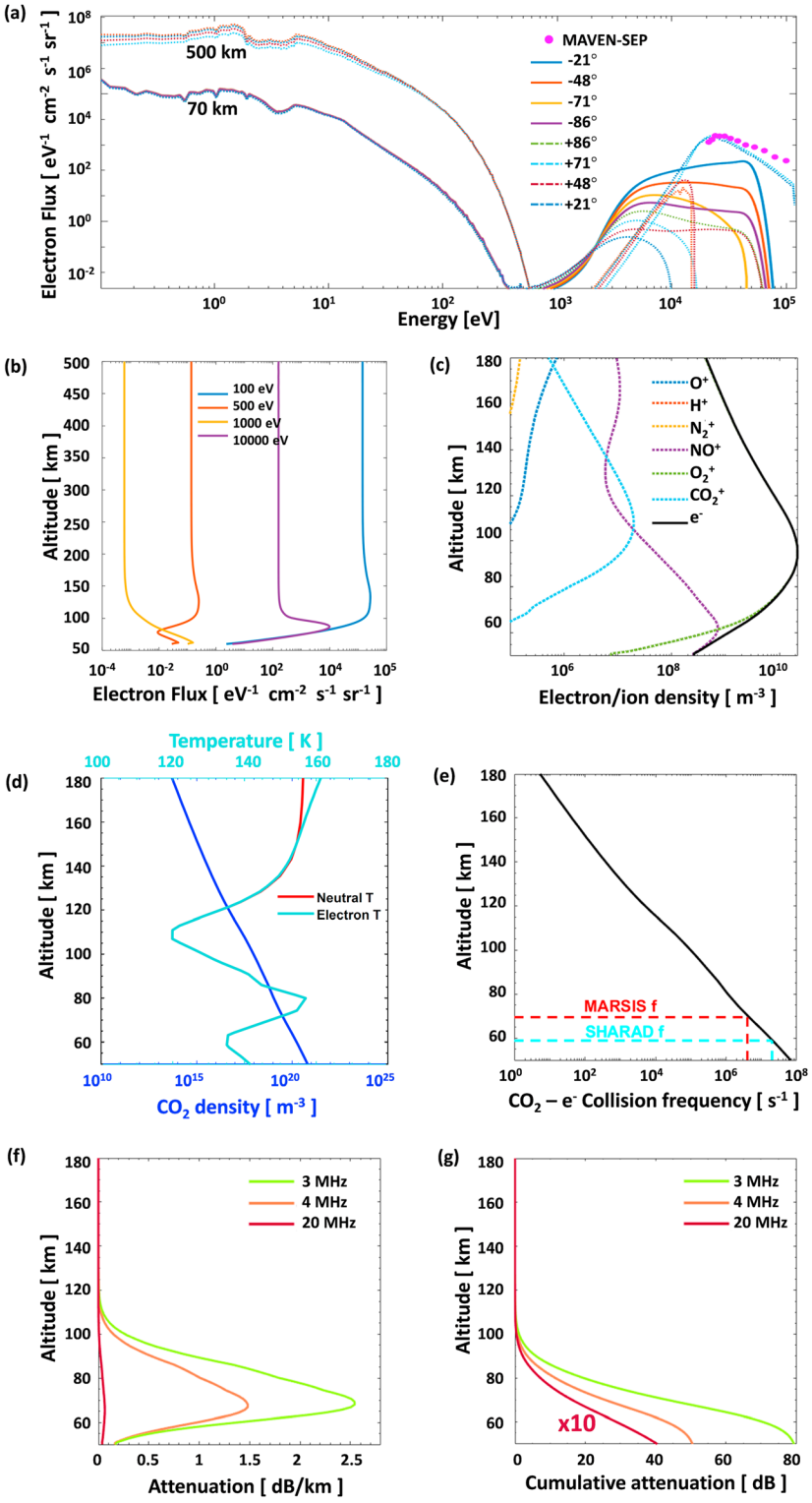

Figure 5. IPIM simulation results. (a) Electron flux as a function of energy at 500 and 70 km. A positive angle means downward flux, and a negative, upward flux. (b) Electron flux profile as a function of altitude for four different energies. (c) Electron density and main ions altitude profiles. (d) Electron and neutral temperatures and CO_2 density profiles with altitude. (e) Electron-CO_2 collision frequency. The altitude at which the MARSIS and SHARAD frequencies equal the collision frequency are indicated with dashed lines. (f) Attenuation profiles with altitude for each radar frequency. (g) Same as in (f) but shown as a cumulative integration. We note that the cumulative attenuation for 20 MHz has been multiplied by the factor 10 for better visualization.

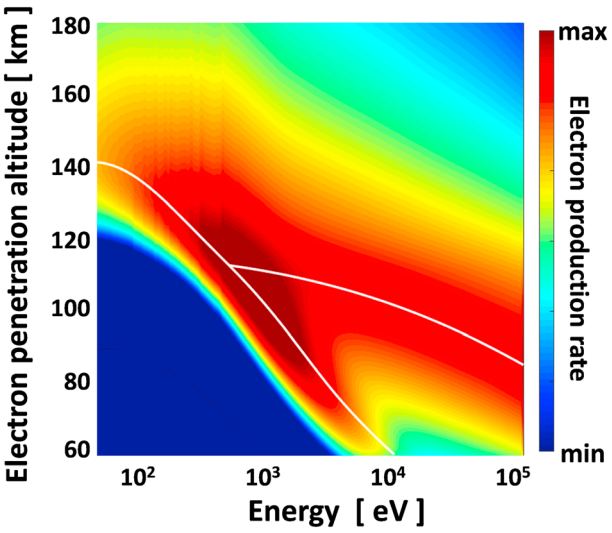

Figure 6. Electron penetration depth versus energy. The while line indicates the altitude where the precipitating electrons are stopped. The upper white line at energy >500 eV is related to secondary electrons, while the lower one is related to the primary electrons.

SEP observations; Figure 5a), we clearly see a low-energy contribution (below 500 eV) present at all altitudes resulting from secondary electrons created by collisions on neutrals. This is also observed when plotting the flux profile with altitude. Figure 5b shows the flux profile of four selected energies in Figure 5a. Large energies, such as 10 keV, have a primary contribution to the atmosphere around ~90–100 km. However, lower energies such as 500 eV, as said before, have two kinds of contributions: a direct one above 100 km and a secondary one caused by secondary electron production at ~60–70 km.

Figure 6 shows the electron penetration depth as a function of energy. It was obtained by calculating the electron production rate associated with a mono-energetic beam of electron precipitation flux for energy in the range 50 eV–100 keV, and then assuming that the altitude for which the electron production rate reaches a maximum (white line) corresponds to the altitude where the precipitating electrons are stopped (Rees, 1989). For energies higher than 500 eV, the white line is split into two as particles are deposited at two different altitudes: the lower one corresponds to direct penetration of the very energetic population, while the upper one is caused by secondary electron production in the atmosphere. This figure indicates that electrons of energy 10 keV are able to penetrate at least down to 60 km. By using a precipitation flux fitted on MAVEN-SEP data, we get the ion density profiles shown in Figure 5c. The simulation predicts that precipitation of energetic electrons created a layer mainly composed by O_2^+, and NO^+ below ~60 km, with a maximum density of ~10^{10} m^{-3} at ~90 km. The width of the layer corresponds to the split discussed in Figure 6. The altitude of this layer agrees well with previous observations of the nightside ionosphere using the radio science technique when solar energetic particle precipitation occurred, although not as intense as for this event. However, the magnitude of the simulation layer for this event is several orders of magnitude larger than the previous nightside observations (Withers et al., 2012) because of the larger precipitating fluxes. The density of this simulated layer is comparable to densities of the dayside ionospheric secondary peak, which is typically found at 110 km (e.g., Sánchez-Cano et al., 2013, 2016).

The radar attenuation caused by this layer was then estimated using the simulation outputs. Figure 5e shows the ν profile obtained from equation (4), and the modeled electron and neutral temperatures (cyan and red, respectively) and CO_2 density (blue) in Figure 5d. The simulation solves the energy balance for thermal electrons and the electron temperature profile results mainly from the thermal equilibrium between cooling by neutrals and ions and heating by suprathermal electrons. The ν profile is in very good agreement with previous estimates (e.g., Nielsen et al., 2007; Witasse et al., 2001). To a first approximation, Figure 5e also shows at which altitude range each radar frequency will suffer its largest attenuation (i.e., when f equals ν). For MARSIS (4 MHz), the attenuation is more efficient at ~70 km, while it is at ~58 km for SHARAD (20 MHz). Finally, Figure 5f shows the attenuation profiles with altitude for three different frequencies, based on equations (2)–(4), and on Figures 5c–5e. All of them peak at ~70 km. Another way of showing these results is in the form of cumulative attenuation profiles, as in Figure 5g. The total attenuation for each f is obtained by integrating each attenuation profile in Figure 5f, giving 79, 50, and 4 dB attenuation for 3, 4, and 20 MHz, respectively. Therefore, the attenuation caused by the lower ionospheric layer was large enough to cause the radar attenuation measured by MARSIS, and of the same order of the attenuation measured by SHARAD (section 3.2).

In order to determine the minimum ionization which is able to produce a signal loss at a certain height, we have estimated how much the total attenuation varies with small changes in density and altitude. Figure 7 left panel shows the total attenuation behavior with frequency for a N_e profile with the same peak density and shape as in Figure 5c but formed at different altitudes (color-coded). For reference, the measured MARSIS and SHARAD attenuations are also indicated. The total attenuation is larger for smaller frequencies as expected, and also, for lower peak altitudes. For MARSIS, the attenuation caused by a layer with magnitude ~10^{10} m^{-3} and similar shape to Figure 5c at 100 km (or lower) would be sufficient to explain the radar

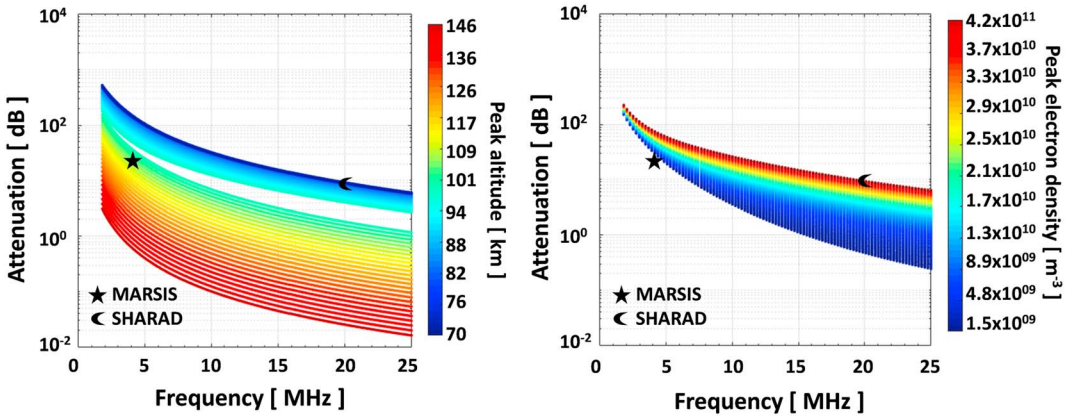

Figure 7. (left panel) Total attenuation versus radar frequency for the electron density profile of Figure 5c at different altitudes. (right panel) Total attenuation versus radar frequency for different electron density peak values of profile of Figure 5c. A star indicates the estimated lower bound on MARSIS attenuation, and the crescent marks the attenuation measured for SHARAD.

blackout. For SHARAD, it would be sufficient if it were below 85 km. Figure 7 right panel shows the total attenuation behavior with frequency for a N_e profile with the same peak altitude and shape as in Figure 5 c but formed with different peak densities (color-coded). As before, the total attenuation is larger for lower frequencies, and in this case, for higher peak densities. For MARSIS, the attenuation caused by a layer of magnitude 3.5×10^9 m^{-3} (or higher) at 90 km would be sufficient to explain the radar blackout. For SHARAD, it would be sufficient with 4.2×10^{11} m^{-3}.

6. Discussion

It is generally accepted that during a SEP event, nightside electron densities are substantially enhanced, and consequently, surface reflections from radar wave propagation tend to disappear (e.g., Espley et al., 2007; Němec et al., 2014). However, these absorbing ionospheric layers formed at low altitude have never been directly measured at Mars, making the estimates of their main characteristics difficult. One of the major difficulties is to understand the cause of the long duration of these blackouts (several days) because the lifetime of the main ionospheric ion, O_2^+, is of the order of a few minutes due to fast dissociative recombination with electrons (Bones et al., 2015). Therefore, the ionization source must be continuous in all these cases for a level of several days, which is rare for a space weather event. An alternative interpretation of these events is that the layer is composed of metallic ions such as Mg^+ and Fe^+, as in sporadic layers in the terrestrial lower *E* region (Plane, 2003). These atomic ions have a relatively long lifetime against neutralization because radiative recombination with electrons is relatively slow, so they first need to form molecular ions (Plane et al., 2018). Mg^+ ions have been continuously observed at Mars by the Imaging Ultraviolet Spectrograph (IUVS) instrument on MAVEN in a layer peaking around 90–95 km and with a typical concentration of $4–8 \times 10^8$ m^{-3} (Crismani et al., 2017). Moreover, a recent model has shown that Mg^+ should be the major form of magnesium above 80 km (Plane et al., 2018, Figure 7), and thus, additional Mg^+ would be unlikely to be produced by SEP from neutral Mg species, either directly or by charge transfer with O_2^+. In fact, the IUVS instrument did not observe a significant increase of Mg^+ during September 2017 (M. Crismani, NASA Goddard Space Flight Center, personal communication). This corroborates that O_2^+ and possibly NO^+ are indeed the main ions that formed the layer.

In the case of space weather events, it is not clear whether the main sources of ionization are solar wind electrons or protons. Most of the previous studies suggested that energetic solar wind protons seem to be responsible (e.g., Morgan et al., 2006; Němec et al., 2015; Sheel et al., 2012). However, Ulusen et al. (2012) found that in four of the six events that they studied, an increase in electron density below 100 km occurred caused by electrons of 10–20 keV energy, which is consistent with the event in the present study. Considering that the ionization source must be continuous in order to explain the long life-time duration of the absorption O_2^+ layer below 100 km, Figure 2 shows that only the continuous enhanced SEP electron flux for ~10 days is able to explain all the radar blackouts seen by both spacecraft because the SEP ion flux was very low

(nearly the same level as that before the space weather event hit Mars) during some periods where blackouts were observed, like for example on the 18–20 September period. Moreover, it was demonstrated with the ionospheric simulation (see Figure 5) in which a precipitation electron flux with the same characteristics as during this event was included. Of course an enhanced SEP proton flux could have contributed to even larger ionization levels, should their flux be high enough. Moreover, the radar attenuation could have been increased by the fact that the nightside electron precipitation was larger over crustal magnetic field regions. However, we note that SHARAD also suffered blackouts while sampling the northern hemisphere (far from crustal fields; see Figure 1 and supporting information), and MARSIS while sampling nonmagnetized areas (such as longitudes ~0–90°; see Figure 1 and supporting information).

Another question to discuss is the fact that energetic particles from the solar wind end up impacting on the nightside atmosphere of Mars. The MAVEN mission has revealed that diffuse aurora can be found at any location on the Martian nightside and is caused by SEPs, specifically electrons accelerated to energies of ~100 keV at the Sun and heliospheric shock fronts (Schneider et al., 2015). For the time period of this study in September 2017, a 25 times brighter diffuse aurora was observed and detectable over the entire visible nightside. Schneider et al. (2018) showed that this aurora emission was originated from an altitude of ~60 km in the atmosphere, which agrees well with the altitude in which the radio signals of both MARSIS and SHARAD radars were lost.

As shown in Figure 2, MARSIS operated in the active ionospheric mode during one orbit when the ICME was transiting Mars. Harada et al. (2018) reported that during this event the nightside peak electron density increased to unusually high values of ~1–2 $\times$ 10^{10} m^{-3} at around 120 km. The magnitude of this reported layer is of the same order as our model results in Figure 5c. However, the reported altitude of the maximum peak is ~30 km higher than our simulations. A possible reason for this altitude discrepancy is that the electron flux in the simulation includes suprathermal electrons that are produced by high-energy precipitating electrons above 20 keV. Since lower energy precipitating electrons are not considered, we lack secondary electrons of energy typically in the energy range 100–1,000 eV which would produce ions at altitudes higher than 100 km (see Figure 5). Therefore, our simulation should be considered as a low-limit estimation for altitudes larger than 100 km, where more ionization could have occurred. Nevertheless, higher-altitude ionization does not significantly change the radio absorption profile, which is the main focus of this paper. Another possible reason could be due to the process of deriving altitudes from MARSIS-AIS data, which is not straightforward (e.g., Morgan et al., 2013; Sánchez-Cano et al., 2012, 2013). In particular, the local plasma density measured at the spacecraft is needed for the computation of the altitude profile on the nightside, which is usually difficult to assess, giving uncertainties of tens of kilometers (Andrews et al., 2013; Morgan et al., 2013). This question will be addressed in a future study.

Finally, attenuation estimates from this study agree well with previous theoretical (Witasse et al., 2001; Withers, 2011) and empirical studies (Espley et al., 2007; Morgan et al., 2006; Nielsen et al., 2007), although we note that all of them were related to dayside or post-terminator regions rather than the deep nightside where our observations come from.

7. Conclusions

We have reported a long HF radar blackout, as shown in the data of the two current radars operating at Mars, MARSIS and SHARAD, during the strong space weather event in September 2017 (Lee et al., 2018). Our interpretation is that the loss of signal is due to the formation of a lower ionospheric layer that absorbed HF radar waves, similar to polar cap absorption or *D*-layer absorption processes on Earth. Modeling shows that this ionospheric layer, created by SEP electrons, rather than previously proposed SEP protons, has a density of ~10^{10} m^{-3} peaking at 90 km, and is mainly composed of O_2^+ with a lesser contribution of NO^+.

This work allows us to identify the need for careful assessments of radar performances for future operational systems. Since these low ionospheric layers produce radar signal losses at least between 3 and 20 MHz, the outcome of this work allows a better assessment of high-frequency radar performances during future space weather events. In those cases, a good characterization of the low ionosphere is necessary for radar operations (and other instruments that use HF radio links), operational planning, and for communications with the Martian surface in the HF range. This case also gives the possibility for the radar teams to flag the quality of data for the legacy archive.

Acknowledgments

B.S.-C., M.L., and S.E.M. acknowledge support through STFC grant ST/N000749/1. ESA-ESTEC Faculty is gratefully acknowledged. F.L. was supported by CNES "Système Solaire" program and by the Programme National de Planétologie and by the ANR (ANR-09-BLAN-0223) and ANR MARMITE (ANR-13-BS05-0012-02). IPIM model simulations can be freely requested at IRAP-CDPP web (http://transplanet.irap.omp.eu/). IPIM model is a property of CNRS. Part of this work and IPIM are supported by the Programme National Soleil Terre (PNST) from Institut des Sciences de l'Univers of Centre National de la Recherche Scientifique (INSU/CNRS) co-funded by CNES. This work was granted access to the HPC resources of CALMIP supercomputing center under the allocation 2017-P1520. Authors thank Matteo Crismani, Wlodek Kofman, and Cyril Grima for the useful discussions. MEX data can be downloaded from the ESA-PSA archive, and MRO and MAVEN data from the NASA-PDS archive.

References

Andrews, D. J., Barabash, S., Edberg, N. J. T., Gurnett, D. A., Hall, B. E. S., Holmström, M., et al. (2016). Plasma observations during the Mars atmospheric "plume" event of March–April 2012. *Journal of Geophysical Research: Space Physics*, *121*, 3139–3154. https://doi.org/10.1002/2015JA022023

Andrews, D. J., Opgenoorth, H. J., Edberg, N. J. T., Andre, M., Franz, M., Dubinin, E., et al. (2013). Determination of local plasma densities with the MARSIS radar: Asymmetries in the high-altitude Martian ionosphere. *Journal of Geophysical Research: Space Physics*, *118*, 6228–6242. https://doi.org/10.1002/jgra.50593

Blelly, P. L., Lathuillère, C., Emery, B., Lilensten, J., Fontanari, J., & Alcaydé, D. (2005). An extended TRANSCAR model including ionospheric convection: Simulation of EISCAT observations using inputs from AMIE. *Annales de Geophysique*, *23*(2), 419–431. https://doi.org/10.5194/angeo-23-419-2005

Blelly, P.-L., Lilensten, J., Robineau, A., Fontanari, J., & Alcayde, D. (1996). Calibration of a numerical ionospheric model with EISCAT observations. *Annales de Geophysique*, *14*(12), 1375–1390. https://doi.org/10.1007/s005850050399

Blelly, P.-L., Marchaudon, A., Indurain, M., Witasse, O., Amaya, J., Chide, B., et al. (2019). Transplanet: A web service dedicated to modeling of planetary ionospheres. *Planetary and Space Science*, ISSN 0032-0633, *169*, 35–44. https://doi.org/10.1016/j.pss.2019.02.008

Bones, D., Plane, J. M. C., & Feng, W. (2015). Dissociative recombination of FeO^+ with electrons: Implications for plasma layers in the ionosphere. *The Journal of Physical Chemistry. A*, *120*(9), 1369–1376. https://doi.org/10.1021/acs.jpca.5b04947

Campbell, B. A., Putzig, N. E., Foss, F. J., & Phillips, R. J. (2014). SHARAD signal attenuation and delay offsets due to the Martian ionosphere. *IEEE Geoscience and Remote Sensing Letters*, *11*(3), 632–635. https://doi.org/10.1109/LGRS.2013.2273396

Cartacci, M., Amata, E., Cicchetti, A., Noschese, R., Giuppi, S., Langlais, B., et al. (2013). Mars ionosphere total electron content analysis from MARSIS subsurface data. *Icarus*, *223*(1), 423–437. https://doi.org/10.1016/j.icarus.2012.12.011

Cartacci, M., Sánchez-Cano, B., Orosei, R., Noschese, R., Cicchetti, A., Witasse, O., et al. (2018). Improved estimation of Mars ionosphere total electron content. *Icarus*, *299*, 396–410. https://doi.org/10.1016/j.icarus.2017

Chicarro, A., Martin, P., & Traunter, R. (2004). *Mars Express: A European Mission to the Red Planet SP-1240*, (pp. 3–16). Noordwijk, Netherlands: Eur. Space Agency Publ. Div.

Crismani, M. M., Schneider, N. M., Plane, J. M., Evans, J. S., Jain, S. K., Chaffin, M. S., et al. (2017). Detection of a persistent meteoric metal layer in the Martian atmosphere. *Nature Geoscience*, *10*(6), 401–404. https://doi.org/10.1038/ngeo2958

Edberg, N. J. T., Lester, M., Cowley, S. W. H., & Eriksson, A. I. (2008). Statistical analysis of the location of the Martian magnetic pileup boundary and bow shock and the influence of crustal magnetic fields. *Journal of Geophysical Research*, *113*(A8), A08206. https://doi.org/10.1029/2008JA013096

Eparvier, F. G., Chamberlin, P. C., Woods, T. N., & Thiemann, E. M. B. (2015). The solar extreme ultraviolet monitor for MAVEN. *Space Science Reviews*, *195*(1-4), 293–301. https://doi.org/10.1007/s11214-015-0195-2

Espley, J. R., Farrell, W. M., Brain, D. A., Morgan, D. D., Cantor, B., Plaut, J. J., et al. (2007). Absorption of MARSIS radar signals: Solar energetic particles and the daytime ionosphere. *Geophysical Research Letters*, *34*, L09101. https://doi.org/10.1029/2006GL028829

Fillingim, M. O., Peticolas, L. M., Lillis, R. J., Brain, D. A., Halekas, J. S., Mitchell, D. L., et al. (2007). Model calculations of electron precipitation induced ionization patches on the nightside of Mars. *Geophysical Research Letters*, *34*, L12101. https://doi.org/10.1029/2007GL029986

Forget, F., Hourdin, F., Fournier, R., Hourdin, C., Talagrand, O., Collins, M., et al. (1999). Improved general circulation models of the Martian atmosphere from the surface to above 80 km. *Journal of Geophysical Research*, *104*(E10), 24,155–24,175. https://doi.org/10.1029/1999JE001025

Fox, J. L., Brannon, J. F., & Porter, H. S. (1993). Upper limits to the nightside ionosphere of Mars. *Geophysical Research Letters*, *20*(13), 1339–1342. https://doi.org/10.1029/93GL01349

Girazian, Z., Mahaffy, P., Lillis, R. J., Benna, M., Elrod, M., Fowler, C. M., & Mitchell, D. L. (2017). Ion densities in the nightside ionosphere of Mars: Effects of electron impact ionization. *Geophysical Research Letters*, *44*, 11,248–11,256. https://doi.org/10.1002/2017GL075431

Girazian, Z., Mahaffy, P. R., Lillis, R. J., Benna, M., Elrod, M., & Jakosky, B. M. (2017). Nightside ionosphere of Mars: Composition, vertical structure, and variability. *Journal of Geophysical Research: Space Physics*, *122*, 4712–4725. https://doi.org/10.1002/2016JA023508

Guo, J., Dumbovic, M., Wimmer-Schweingruber, R. F., Temmer, M., Lohf, H., Wang, Y., et al. (2018). Modeling the evolution and propagation of the 2017 September 9th and 10th CMEs and SEPs arriving at Mars constrained by remote-sensing and in-situ measurement. *Space Weather*, *16*, 1156–1169. https://doi.org/10.1029/2018SW001973

Hall, B. E. S., Lester, M., Sánchez-Cano, B., Nichols, J. D., Andrews, D. J., Edberg, N. J. T., et al. (2016). Annual variations in the Martian bow shock location as observed by the Mars express mission. *Journal of Geophysical Research: Space Physics*, *121*, 11,474–11,494. https://doi.org/10.1002/2016JA023316

Harada, Y., Gurnett, D. A., Kopf, A. J., Halekas, J. S., Ruhunusiri, S., DiBraccio, G. A., et al. (2018). MARSIS observations of the Martian nightside ionosphere during the September 2017 solar event. *Geophysical Research Letters*, *45*(16), 7960–7967. https://doi.org/10.1002/2018GL077622

Itikawa, Y. (1978). Momentum transfer cross sections for electron collisions with atoms and molecules. *Atomic Data and Nuclear Data Tables*, *21*(1), 69–75. https://doi.org/10.1016/0092-640X(78)90004-9

Jiggens, P., Clavie, C., Evans, H., O'Brien, T. P., Witasse, O., Mishev, A. L., et al. (2018). In-situ data and effect correlation during September 2017 solar particle event. *Space Weather*, *17*, 99–117. https://doi.org/10.1029/2018SW001936

Larson, D., Lillis, R. J., Lee, C. O., Dunn, P. A., Hatch, K., Robinson, M., et al. (2015). The MAVEN solar energetic particle investigation. *Space Science Reviews*, *195*(1-4), 153–172. https://doi.org/10.1007/s11214-015-0218-z

Leblanc, F., Witasse, O., Winningham, J., Brain, D., Lilensten, J., Blelly, P.-L., et al. (2006). Origins of the Martian aurora observed by Spectroscopy for Investigation of Characteristics of the Atmosphere of Mars (SPICAM) on board Mars Express. *Journal of Geophysical Research*, *111*(A9), A09313. https://doi.org/10.1029/2006JA011763

Lee, C. O., Jakosky, B. M., Luhmann, J. G., Brain, D. A., Mays, M. L., Hassler, D. M., et al. (2018). Observations and impacts of the 10 September 2017 solar events at Mars: An overview and synthesis of the initial results. *Geophysical Research Letters*, *45*(17), 8871–8885. https://doi.org/10.1029/2018GL079162

Lillis, R. J., & Fang, X. (2015). Electron impact ionization in the Martian atmosphere: Interplay between scattering and crustal magnetic field effects. *Journal of Geophysical Research: Planets*, *120*, 1332–1345. https://doi.org/10.1002/2015JE004841

Lillis, R. J., Fillingim, M. O., & Brain, D. A. (2011). Three-dimensional structure of the Martian nightside ionosphere: Predicted rates of impact ionization from Mars Global Surveyor MAG/ER measurements of precipitating electrons. *Journal of Geophysical Research*, *116*(A12), A12317. https://doi.org/10.1029/2011JA016982

Lillis, R. J., Mitchell, D. L., Steckiewicz, M., Brain, D., Xu, S., Weber, T., et al. (2018). Ionizing electrons on the Martian nightside: Structure and variability. *Journal of Geophysical Research: Space Physics*, *123*(5), 4349–4363. https://doi.org/10.1029/2017JA025151

Marchaudon, A., & Blelly, P.-L. (2015). A new 16-moment interhemispheric model of the ionosphere: IPIM. *Journal of Geophysical Research: Space Physics*, *120*, 5728–5745. https://doi.org/10.1002/2015JA021193

Millour, E., Forget, F., Spiga, A., Navarro, T., Madeleine, J.-B., Montabone, L., et al. (2015). The Mars Climate Database (MCD version 5.2), in European Planetary Science Congress 2015, vol. 10, EPSC2015–438, Nantes, France, 27 Sept.–2 Oct.

Molina-Cuberos, G. J., Witasse, O., Lebreton, J.-P., Rodrigo, R., & Lopez-Moreno, J. J. (2003). Meteoric ions in the atmosphere of Mars. *Planetary and Space Science*, *51*(3), 239–249. https://doi.org/10.1016/S0032-0633(02)00197-6

Morel, L., Witasse, O., Warnant, R., Cerisier, J.-C., Blelly, P.-L., & Lilensten, J. (2004). Diagnostic of the dayside ionosphere of Mars using the total electron content measurement by the NEIGE/Netlander experiment: An assessment study. *Planetary and Space Science*, *52*(7), 603–611. https://doi.org/10.1016/j.pss.2003.12.007

Morgan, D. D., Diéval, C., Gurnett, D. A., Duru, F., Dubinin, E. M., Fränz, M., et al. (2014). Effects of a strong ICME on the Martian ionosphere as detected by Mars Express and Mars Odyssey. *Journal of Geophysical Research: Space Physics*, *119*, 5891–5908. https://doi.org/10.1002/2013JA019522

Morgan, D. D., Gurnett, D. A., Kirchner, D. L., David Winningham, J., Frahm, R. A., Brain, D. A., et al. (2010). Radar absorption due to a corotating interaction region encounter. *Icarus*, *206*(1), 95–103. https://doi.org/10.1016/j.icarus.2009.03.008

Morgan, D. D., Gurnett, D. A., Kirchner, D. L., Huff, R. L., Brain, D. A., Boyton, W. V., et al. (2006). Solar control of radar wave absorption by the Martian ionosphere. *Geophysical Research Letters*, *33*, L13202. https://doi.org/10.1029/2006GL026637

Morgan, D. D., Witasse, O., Nielsen, E., Gurnett, D. A., Duru, F., & Kirchner, D. L. (2013). The processing of electron density profiles from the Mars Express MARSIS topside sounder. *Radio Science*, *48*, 197–207. https://doi.org/10.1002/rds.20023

Mouginot, J., Kofman, W., Safaeinili, A., & Herique, A. (2008). Correction of the ionospheric distortion on the MARSIS surface sounding echoes. *Planetary and Space Science*, *56*(7), 917–926. https://doi.org/10.1016/j.pss.2008.01.010

Němec, F., Morgan, D. D., Dieval, C., & Gurnett, D. A. (2015). Intensity of nightside MARSIS AIS surface reflections and implications for low-altitude ionospheric densities. *Journal of Geophysical Research: Space Physics*, *120*, 3226–3239. https://doi.org/10.1002/2014JA020888

Němec, F., Morgan, D. D., Dieval, C., Gurnett, D. A., & Futaana, Y. (2014). Enhanced ionization of the Martian nightside ionosphere during solar energetic particle events. *Geophysical Research Letters*, *41*, 793–798. https://doi.org/10.1002/2013GL058895

Nielsen, E., Morgan, D. D., Kirchner, D. L., Plaut, J. J., & Picardi, G. (2007). Absorption and reflection of radio waves in the Martian ionosphere. *Planetary and Space Science*, *55*(7-8), 864–870. https://doi.org/10.1016/j.pss.2006.10.005

Orosei, R., Jordan, R. L., Morgan, D. D., Cartacci, M., Cicchetti, A., Duru, F., et al. (2015). Mars Advanced Radar for Subsurface and Ionospheric Sounding (MARSIS) after nine years of operation: A summary. *Planetary and Space Science*, *112*, 98–114. https://doi.org/10.1016/j.pss.2014.07.010

Pesnell, W. D., & Grebowsky, J. (2000). Meteoric magnesium ions in the Martian atmosphere. *Journal of Geophysical Research*, *105*(E1), 1695–1707. https://doi.org/10.1029/1999JE001115

Picardi, G., Biccari, D., Seu, R., Plaut, J., Johnson, W. T. K., Jordan, R. L., et al. (2004). MARSIS: Mars advanced radar for subsurface and ionosphere sounding. In A. Wilson, & A. Chicarro (Eds.), *Mars Express: The scientific payload*, Special Publication, (Vol. *1240*, pp. 51–69). Noordwijk, Netherlands: ESA.

Plane, J. M. C. (2003). Atmospheric chemistry of meteoric metals. *Chemical Reviews*, *103*(12), 4963–4984. https://doi.org/10.1021/cr0205309

Plane, J. M. C., Carrillo-Sanchez, J. D., Mangan, T. P., Crismani, M. M. J., Schneider, N. M., & Määttänen, A. (2018). Meteoric metal chemistry in the Martian atmosphere. *Journal of Geophysical Research: Planets*, *123*(3), 695–707. https://doi.org/10.1002/2017JE005510

Ramírez-Nicolás, B., Sánchez-Cano, O., Witasse, P.-L., Blelly, L., & Vázquez, M. L. (2016). The effect of the induced magnetic field on the electron density vertical profile of the Mars' ionosphere: A Mars Express MARSIS radar data analysis and interpretation, a case study. *Planetary and Space Science*, *126*, 49–62. https://doi.org/10.1016/j.pss.2016.03.017

Redmon, R. J., Seaton, D. B., Steenburgh, R., He, J., & Rodriguez, J. V. (2018). September 2017's geoeffective space weather and impacts to Caribbean radio communications during hurricane response. *Space Weather*, *16*, 1190–1201. https://doi.org/10.1029/2018SW001897

Rees, M. (1989). The interaction of energetic electrons and ions with the upper atmosphere. In *Physics and Chemistry of the Upper Atmosphere (Cambridge Atmospheric and Space Science Series, Chapter 3)*. Cambridge: Cambridge University Press. https://doi.org/10.1017/CBO9780511573118.004

Safaeinili, A., Kofman, W., Mouginot, J., Gim, Y., Herique, A., Ivanov, A. B., et al. (2007). Estimation of the total electron content of the Martian ionosphere using radar sounder surface echoes. *Geophysical Research Letters*, *34*, L23204. https://doi.org/10.1029/2007GL032154

Safaeinili, A., Kofman, W., Nouvel, J., Herique, A., & Jordan, R. L. (2003). Impact of Mars ionosphere on orbital radar sounder operation and data processing. *Planetary and Space Science*, *51*(7-8), 505–515. https://doi.org/10.1016/S0032-0633(03)00048-5

Sánchez-Cano, B., Lester, M., Witasse, O., Blelly, P.-L., Indurain, M., Cartacci, M., et al. (2018). Spatial, seasonal, and solar cycle variations of the Martian total electron content (TEC): Is the TEC a good tracer for atmospheric cycles? *Journal of Geophysical Research: Planets*, *123*(7), 1746–1759. https://doi.org/10.1029/2018JE005626

Sánchez-Cano, B., Lester, M., Witasse, O., Milan, S. E., Hall, B. E. S., Blelly, P.-L., et al. (2015). Evidence of scale height variations in the Martian ionosphere over the solar cycle. *Journal of Geophysical Research: Space Physics*, *120*, 10,913–10,925. https://doi.org/10.1002/2015JA021949

Sánchez-Cano, B., Lester, M., Witasse, O., Milan, S. E., Hall, B. E. S., Cartacci, M., et al. (2016). Solar cycle variations in the ionosphere of Mars as seen by multiple Mars Express data sets. *Journal of Geophysical Research: Space Physics*, *121*, 2547–2568. https://doi.org/10.1002/2015JA022281

Sánchez-Cano, B., Morgan, D. D., Witasse, O., Radicella, S. M., Herraiz, M., Orosei, R., et al. (2015). Total electron content in the Martian atmosphere: A critical assessment of the Mars Express MARSIS data sets. *Journal of Geophysical Research: Space Physics*, *120*, 2166–2182. https://doi.org/10.1002/2014JA020630

Sánchez-Cano, B., Radicella, S. M., Herraiz, M., Witasse, O., & Rodríguez-Caderot, G. (2013). NeMars: An empirical model of the Martian dayside ionosphere based on Mars Express MARSIS data. *Icarus*, *225*(1), 236–247. https://doi.org/10.1016/j.icarus.2013.03.021

Sánchez-Cano, B., Witasse, O., Herraiz, M., Radicella, S. M., Bauer, J., Blelly, P.-L., & Rodríguez-Caderot, G. (2012). Retrieval of ionospheric profiles from the Mars Express MARSIS experiment data and comparison with radio-occultation data. *Geoscientific Instrumentation, Methods and Data Systems*, *1*(1), 77–84. https://doi.org/10.5194/gi-1-77-2012

Schneider, N. M., Deighan, J. I., Jain, S. K., Stiepen, A., Stewart, A. I. F., Larson, D., et al. (2015). Discovery of diffuse aurora on Mars. *Science*, *350*(6261), aad0313. https://doi.org/10.1126/science.aad0313

Schneider, N. M., Jain, S. K., Deighan, J., Nasr, C. R., Brain, D. A., Larson, D., et al. (2018). Global aurora on Mars during the September 2017 space weather event. *Geophysical Research Letters*, *45*(15), 7391–7398. https://doi.org/10.1029/2018GL077772

Schunk, R., & Nagy, A. F. (2009). *Ionospheres: Physics, plasma physics, and chemistry*. New York: Cambridge Univ. Press. https://doi.org/10.1017/CBO9780511635342

Seu, R., Biccardi, D., Orosei, R., Lorenzoni, L. V., Phillips, R. J., Marinangeli, L., et al. (2004). SHARAD: The MRO 2005 shallow radar. *Planetary and Space Science*, *52*(1-3), 157–166. https://doi.org/10.1016/j.pss.2003.08.024

Sheel, V., Haider, S. A., Withers, P., Kozarev, K., Jun, I., Kang, S., et al. (2012). Numerical simulation of the effects of a solar energetic particle event on the ionosphere of Mars. *Journal of Geophysical Research*, *117*(A5), A05312. https://doi.org/10.1029/2011JA017455

Ulusen, D., Brain, D. A., Luhmann, J. G., & Mitchell, D. L. (2012). Investigation of Mars' ionospheric response to solar energetic particle events. *Journal of Geophysical Research*, *117*(A12), A12306. https://doi.org/10.1029/2012JA017671

Witasse, O. (2000). Modélisation des Ionosphères planétaires et de leur Rayonnement: La Terre et Mars, PhD thesis, Laboratoire de Planétologie de Grenoble.

Witasse, O., Dutuit, O., Lilensten, J., Thissen, R., Zabka, J., Alcaraz, C., et al. (2002). Prediction of a CO_2^{2+} layer in the atmosphere of Mars. *Geophysical Research Letters*, *29*(8), 1263. https://doi.org/10.1029/2002GL014781

Witasse, O., Dutuit, O., Lilensten, J., Thissen, R., Zabka, J., Alcaraz, C., et al. (2003). Correction to "Prediction of a CO_2^{2}+ layer in the atmosphere of Mars". *Geophysical Research Letters*, *30*(7), 1360. https://doi.org/10.1029/2003GL017007

Witasse, O., Nouvel, J.-F., Lebreton, J.-P., & Kofman, W. (2001). HF radio wave attenuation due to a meteoric layer in the atmosphere of Mars. *Geophysical Research Letters*, *28*(15), 3039–3042. https://doi.org/10.1029/2001GL013164

Withers, P. (2011). Attenuation of radio signals by the ionosphere of Mars: Theoretical development and application to MARSIS observations. *Radio Science*, *46*, RS2004. https://doi.org/10.1029/2010RS004450

Withers, P., Fillingim, M. O., Lillis, R. J., Häusler, B., Hinson, D. P., Tyler, G. L., et al. (2012). Observations of the nightside ionosphere of Mars by the Mars Express Radio Science Experiment (MaRS). *Journal of Geophysical Research*, *117*(A12), A12307. https://doi.org/10.1029/2012JA018185

Zurek, R. W., & Smrekar, S. E. (2007). An overview of the Mars Reconnaissance Orbiter (MRO) science mission. *Journal of Geophysical Research*, *112*(E5), E05S01. https://doi.org/10.1029/2006JE002701